

Diffusion-based G-buffer generation and rendering

BOWEN XUE, University of Manchester, UK

GIUSEPPE CLAUDIO GUARNERA, University of York, UK

SHUANG ZHAO, University of California, Irvine, UK

ZAHRA MONTAZERI, University of Manchester, UK

A bright, spacious modern living room with wooden flooring, featuring a minimalist design. The walls are painted in a neutral gray. There is a comfortable sofa placed in one corner, accompanied by a few potted green plants.



Fig. 1. We propose a novel text-to-image pipeline that begins by generating a G-buffer for any given text prompt. Users can then modify this G-buffer—by copying and pasting within the albedo, roughness, metallic, normal, and depth channels, or by applying masks to the irradiance channel to overwrite specific regions. This process enables operations such as inserting or repositioning objects, as illustrated in the second and third examples. Alternatively, users can render the final image without any manual edits. Leveraging these capabilities, our G-buffer rendering network can seamlessly integrate real objects into virtual scenes or place virtual objects into real scenes.

Despite recent advances in text-to-image generation, controlling geometric layout and material properties in synthesized scenes remains challenging. We present a novel pipeline that first produces a G-buffer (albedo, normals, depth, roughness, and metallic) from a text prompt and then renders a final image through a modular neural network. This intermediate representation enables fine-grained editing: users can copy and paste within specific G-buffer channels to insert or reposition objects, or apply masks to the irradiance channel to adjust lighting locally. As a result, real objects can be seamlessly integrated into virtual scenes, and virtual objects can be placed into real environments with high fidelity. By separating scene decomposition from image rendering, our method offers a practical balance between detailed post-generation control and efficient text-driven synthesis. We demonstrate its effectiveness on a variety of examples, showing that G-buffer editing significantly extends the flexibility of text-guided image generation.

Authors' addresses: Bowen Xue, University of Manchester, UK; Giuseppe Claudio Guarnera, University of York, UK; Shuang Zhao, University of California, Irvine, UK; Zahra Montazeri, University of Manchester, UK.

Permission to make digital or hard copies of all or part of this work for personal or classroom use is granted without fee provided that copies are not made or distributed for profit or commercial advantage and that copies bear this notice and the full citation on the first page. Copyrights for components of this work owned by others than ACM must be honored. Abstracting with credit is permitted. To copy otherwise, or republish, to post on servers or to redistribute to lists, requires prior specific permission and/or a fee. Request permissions from permissions@acm.org.

© 2025 Association for Computing Machinery.

0730-0301/2025/3-ART \$15.00

<https://doi.org/10.1145/nnnnnnnn.nnnnnnnn>

Additional Key Words and Phrases: Image-based Rendering, Diffusion Models, Neural Rendering, Text-to-Image Generation

ACM Reference Format:

Bowen Xue, Giuseppe Claudio Guarnera, Shuang Zhao, and Zahra Montazeri. 2025. Diffusion-based G-buffer generation and rendering. *ACM Trans. Graph.* 1, 1 (March 2025), 10 pages. <https://doi.org/10.1145/nnnnnnnn.nnnnnnnn>

1 INTRODUCTION

Text-to-image diffusion models have attracted significant attention due to their ability to produce high-fidelity images from natural language prompts [Ramesh et al. 2021; Rombach et al. 2022; Saharia et al. 2022]. However, many of these models provide limited user control, often forcing iterative re-generation to achieve specific alterations—such as adjusting a scene's layout or modifying material properties. Moreover, once a scene is rendered, introducing further edits at the pixel level becomes challenging without resorting to a complete re-run of the entire generative process.

In this work, we address these challenges by coupling image-based rendering with diffusion modeling. Specifically, our system first generates a G-buffer, including geometric, material, and lighting information (albedo, normals, depth, roughness, metallic, and irradiance), and then uses a neural renderer to produce the final image. This design grants users a more flexible editing interface:

rather than relying solely on text prompts, they can directly manipulate the G-buffer channels to revise lighting or geometry, even after generation. We further adopt a two-stage training strategy that freezes a pre-trained diffusion model initially—preserving its wide-ranging generative capabilities—and integrates a ControlNet component to refine the G-buffer output without overfitting on our smaller, primarily indoor dataset. Subsequently, we fine-tune both the diffusion backbone and the ControlNet with a reduced learning rate to ensure stable convergence and avoid catastrophic forgetting. Additionally, our rendering network applies a modular sub-network approach that separately processes geometry, material, and lighting channels, thereby aligning with physically based rendering principles and yielding more accurate reflections, shadows, and transparency effects.

We experimentally validate our framework on large-scale indoor datasets and show its ability to generalize to outdoor scenarios as well. In addition, we conduct both quantitative evaluations and a user study with 156 participants to assess the perceived realism and editability improvements. Our experiments demonstrate that, compared to conventional text-to-image pipelines, our approach substantially improves control over scene geometry and material attributes while preserving generative diversity.

Contributions:

- **Screen-space rendering Diffusion Pipeline.** We propose a novel two-stage pipeline that first generates a G-buffer from text prompts using a partially frozen diffusion model and ControlNet, then renders the final image with a physically inspired, modular network structure.
- **Enhanced Editability and Generalization.** By employing G-buffers, we enable fine-grained post-generation edits and demonstrate our method’s capacity to handle both indoor and outdoor scenes, despite training primarily on indoor-focused datasets.
- **Preservation of Generative Power.** Our approach freezes the diffusion model’s parameters in the initial training phase to avoid catastrophic forgetting and overfitting, preserving the broad capabilities learned from large-scale pre-training.
- **Modular Sub-Network Rendering.** We introduce separate sub-networks for geometry, material, and shading channels in the rendering stage, improving interpretability, convergence stability, and performance on complex objects such as transparent or reflective materials.

2 RELATED WORK

Text-to-Image Generation. Text-to-image generation has advanced considerably through GANs and diffusion models. Early GAN-based methods demonstrated the feasibility of synthesizing images from textual descriptions but often suffered from low resolution and limited semantic alignment [Reed et al. 2016; Zhang et al. 2017]. Attention-based architectures improved the correlation between text embeddings and visual content [Xu et al. 2018]. In parallel, diffusion models offered better coverage of the data manifold and reduced mode collapse [Dhariwal and Nichol 2021], leading to large-scale systems like DALL-E [Ramesh et al. 2021] and GLIDE [Nichol et al. 2022], which introduced classifier-free guidance. Latent diffusion

approaches enabled high-resolution outputs at reduced cost [Romach et al. 2022], forming the basis of Stable Diffusion, while Imagen further improved photorealistic generation through cascaded diffusion [Saharia et al. 2022]. Despite these advances, post-generation editing of specific scene elements remains challenging.

Screen-Space Rendering. Screen-space rendering bridges purely 2D methods and full 3D reconstructions, capturing partial spatial data via layered depth images or G-buffers [Buehler et al. 2001; Penner and Zhang 2017]. This enables moderate viewpoint changes and scene manipulation without the complexity of volumetric geometry. For instance, Hedman et al. [Hedman et al. 2018] supported free-viewpoint navigation with multi-view blending, while Zhang et al. [Zhang et al. 2024] employed real-time screen space rendering methods for multiphase fluid simulation.. Although not fully volumetric, screen-space techniques encode essential geometric and material attributes (e.g., normals, depth, inferred lighting), allowing efficient re-rendering under varied perspectives. This motivates our strategy of adding a text-to-G-buffer generation phase, combining the compactness of screen-space representations with the adaptability of a generative framework.

Neural Rendering. Neural rendering synthesizes novel views or edited scenes from volumetric or surface-based data, bridging computer graphics and machine learning. NeRFs [Mildenhall et al. 2021] first demonstrated high-fidelity view synthesis by mapping continuous 3D coordinates to density and color, later extended to dynamic scenes [Park et al. 2021], and anti-aliased systems for unbounded environments [Barron et al. 2022]. Surface-based methods [Lombardi et al. 2019; Trevischi et al. 2020] utilize explicit geometry or point-based representations for realistic rendering but often demand substantial data and computation, complicating fine-grained edits. Our pipeline employs screen-space G-buffers within a modular neural architecture, disentangling geometry, material, and irradiance in line with physically based rendering principles. This design balances the fidelity of advanced neural rendering and the interactive flexibility of lightweight screen-space approaches.

Neural Image Synthesis from G-buffer. Several approaches learn image synthesis from screen-space buffers or intermediate decompositions. Deep Shading [Nalbach et al. 2017] infers effects like ambient occlusion and subsurface scattering via CNNs, while Deep Illumination [Thomas and Forbes 2018] employs a conditional GAN to predict global illumination. Zhu et al. [Zhu et al. 2022a] propose screen-space ray tracing from intrinsic channels, and RGBX [Zeng et al. 2024] fine-tunes a Stable Diffusion model to render intermediate decompositions.

Editing and Relighting. Neural relighting can rely on explicit representations [Griffiths et al. 2022; Pandey et al. 2021; Yu et al. 2020] or implicit ones [Rudnev et al. 2022; Wang et al. 2023], typically limited to simpler lighting conditions. Diffusion-handles [Pandey et al. 2024] applies a diffusion-based model for object manipulation. In contrast, our framework supports more general scene edits—such as object insertion, movement, or shading tweaks—without specialized relighting constraints or scene-specific data, providing broader editing capabilities.

3 OUR METHOD

In this section, we describe the overall network architecture design. Traditional diffusion models generate images end-to-end from text but offer weak controllability over the generated images. Multiple attempts may be needed to produce a satisfactory result, and even then, making modifications can be difficult. To address this issue, we combine image-based rendering with diffusion models. We first generate a G-buffer that represents the desired scene and then use a neural network to render the G-buffer. Based on this approach, we designed a segmented network: the first part generates the G-buffer from text, and the second part renders the G-buffer into an image.

3.1 Text to G-buffer Network

In this section, we describe our approach for generating G-buffers (albedo, normal, depth, irradiance, roughness, metallic, etc.) directly from text prompts, leveraging a two-stage diffusion-based network. Our goal is to preserve the large-scale generative capability of Stable Diffusion while adapting it to a smaller, indoor-specific dataset.

Motivation and Overview. We draw inspiration from [Podell et al. 2023; Xue et al. 2024] to design our first-stage network. The key challenge is that our dataset is significantly smaller than the original Stable Diffusion corpus and focuses predominantly on indoor scenes. Directly retraining or fully fine-tuning the diffusion model on such a narrow subset can result in overfitting and catastrophic forgetting of broader content, as shown in Figure 3.

To address this, we use a **two-stage** network design similar to [Xue et al. 2024]. In *Stage 1*, we adopt a *frozen* diffusion model, thereby preserving the pretrained model’s generative capabilities. In *Stage 2*, rather than retraining the diffusion model itself—which can lead to model collapse or chaotic outputs on small datasets—we introduce a **ControlNet** structure. This approach converges more easily and accelerates training. Toward the end of training, we *unfreeze* the main diffusion model, but at a learning rate one-fifth that of ControlNet, further reducing the loss and improving G-buffer results.

Figure 2 provides an overview of our pipeline. First, a text prompt is converted into embeddings and fed into the frozen Stable Diffusion model for denoising. The resulting latent representation is then passed to the second part of the network, which continues denoising and incorporates a trained ControlNet to output the final G-buffer. Users can further edit or render the G-buffer using subsequent networks.

Theoretical Justification. We now illustrate the rationale behind partially freezing the diffusion model and introducing a relatively small ControlNet module, rather than fully fine-tuning all parameters on a small dataset.

Let $\theta^* \in \mathbb{R}^D$ be the parameters of a large diffusion model, pretrained on a massive data distribution $\mathcal{D}_{\text{large}}$. The model encodes an implicit “text-to-latent” mapping:

$$\mathcal{F}^*(x) : x \mapsto \text{image latent}, \quad (1)$$

where x includes text embeddings, diffusion steps, noise, and so forth. Suppose we have a new, *smaller* dataset $S = \{(x_i, y_i)\}_{i=1}^n$ from a distribution \mathcal{D}_{new} , where $n \ll |\mathcal{D}_{\text{large}}|$. Our objective is to adapt

\mathcal{F}^* to this new task/distribution while preserving the capabilities learned during pre-training.

Strategy A: Freeze $\theta^ + \text{ControlNet}$.* We introduce a smaller parameter set $\phi \in \mathbb{R}^M$ (with $M \ll D$) to form a composite function:

$$\mathcal{F}_{\theta^*, \phi}(x) = \mathcal{H}(\mathcal{F}^*(x), g_\phi(x)), \quad (2)$$

where $\mathcal{H}(\cdot, \cdot)$ represents the layer-wise feature injection or merging process across multiple blocks of the UNet.

$$\hat{\phi} = \arg \min_{\phi} \frac{1}{n} \sum_{i=1}^n \ell(\theta^*, \phi; x_i, y_i). \quad (3)$$

Here, θ^* is fixed, so we do *not* risk overwriting its original mapping \mathcal{F}^* .

Strategy B: Fine-tune All UNet Parameters. Alternatively, one might fully unfreeze $\theta \in \mathbb{R}^D$, leading to:

$$\hat{\theta} = \arg \min_{\theta} \frac{1}{n} \sum_{i=1}^n \ell(\theta; x_i, y_i). \quad (4)$$

Because $n \ll D$, this high-capacity model is more prone to overfitting \mathcal{D}_{new} and forgetting the knowledge acquired from $\mathcal{D}_{\text{large}}$.

View 1: Preserving the Learned Latent Function. If \mathcal{D}_{new} is a subset or a variant of $\mathcal{D}_{\text{large}}$, the mapping $\mathcal{F}^*(\cdot)$ in (1) still largely applies. Freezing θ^* thus retains the *bulk* of the pretrained text-to-latent capability, while ϕ in (2) only needs to capture the task-specific (or distribution-shift) refinements. By contrast, fully tuning (4) may drastically deviate from θ^* and destroy prior knowledge.

View 2: Model Capacity and Rademacher Complexity. From the standpoint of statistical learning theory, let $\mathcal{H}_{\text{full}}$ be the hypothesis class when fine-tuning all parameters $\theta \in \mathbb{R}^D$, and let $\mathcal{H}_{\text{ctrl}}$ be the restricted class when freezing θ^* and only optimizing $\phi \in \mathbb{R}^M$. Typically,

$$C(\mathcal{H}_{\text{full}}) \gg C(\mathcal{H}_{\text{ctrl}}),$$

where $C(\cdot)$ denotes a capacity measure (e.g., Rademacher complexity). The corresponding generalization bound

$$|\hat{L}_n(h) - L(h)| \leq \mathcal{O}\left(\frac{C(\mathcal{H})}{\sqrt{n}}\right)$$

is tighter for the smaller hypothesis class $\mathcal{H}_{\text{ctrl}}$. Consequently, *Strategy A* is less prone to overfitting and better preserves the pretrained mapping.

By preserving the pretrained parameters θ^* and introducing a relatively small ControlNet ϕ , we retain the latent function \mathcal{F}^* and confine new adaptations to a lower-dimensional space. This design strategy mitigates catastrophic forgetting and *improves generalization* on small-data tasks compared to fully tuning all D parameters. Figure 3 compares these strategies, showcasing how directly training all Stable Diffusion parameters on a small dataset can degrade its broader generative capability.

3.2 G-buffer Rendering Network

Our G-buffer to image rendering pipeline leverages a fine-tuned Stable Diffusion model with a ControlNet backbone. The ControlNet input consists of 13 stacked channels: albedo, normal, roughness, irradiance, metallic, depth, and a mask. This mask is used to indicate

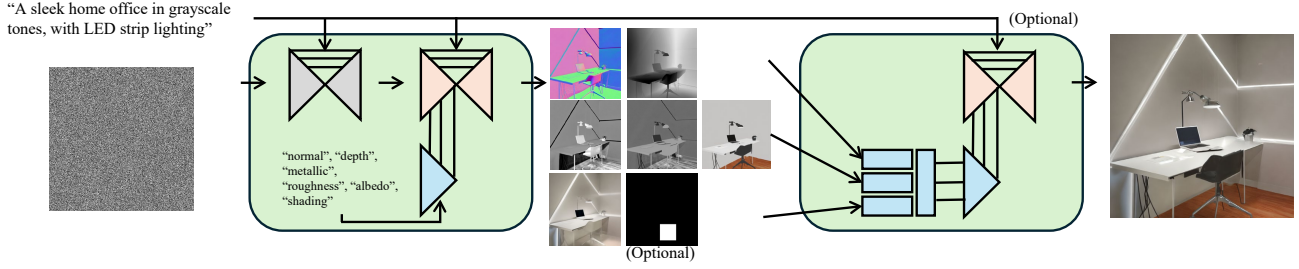


Fig. 2. Overview. Our pipeline begins with a random noise sample and a text prompt. These inputs are processed by the stage-1 network, which consists of two denoising steps: first, a frozen Stable Diffusion 2 model (in gray), followed by a fine-tuned Stable Diffusion 2 model augmented with ControlNet. Stage 1 produces a G-buffer comprising albedo, normal, depth, irradiance, roughness, and metallic. These channels are then grouped and passed to the stage-2 network, where an optional mask is used for object movement or insertion. Each group is processed by specialized sub-networks, fused by a final grouping module, and then fed into another ControlNet-equipped, fine-tuned Stable Diffusion 2 model to generate the final RGB output.

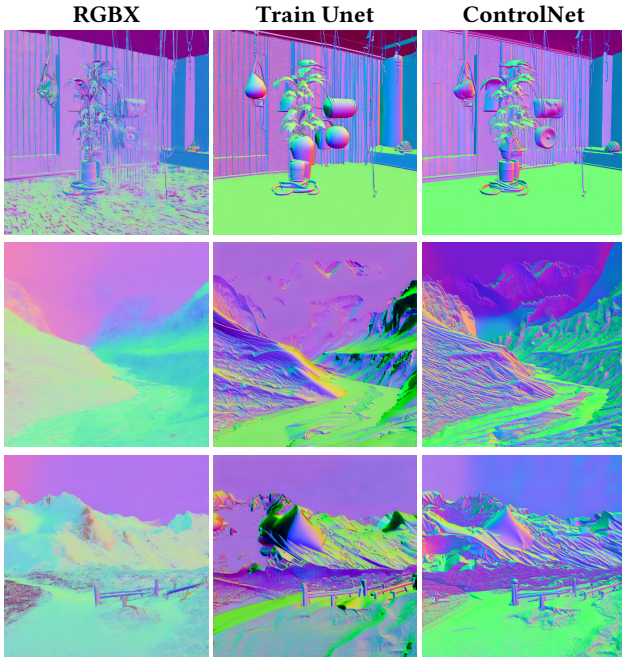


Fig. 3. Text-to-G-buffer Ablation. This figure compares the performance of three text-to-G-buffer generation approaches across three example scenes (rows), with all images depicting normal maps. The first column shows results from linking the RGBX network to the full Stable Diffusion pipeline, using the same noise, seed, and generator as our method. The second column presents outcomes from directly training the Stable Diffusion UNet without ControlNet. The third column showcases results from our full method, demonstrating its superior performance compared to the alternatives.

regions where new objects are inserted or existing objects are moved. In the designated regions, the irradiance channel is zeroed out, while other channels are inherited from the inserted object. Object insertion remains optional; if no object is inserted, the mask is set to 1 everywhere.

However, the original ControlNet design assumes a three-channel conditional input. Simply concatenating additional channels tends

to cause poor performance and training instability. Moreover, our extra channels are not just additional color images but a more complex, multi-component G-buffer. Hence, we prepend a multi-layer CNN module to ControlNet to extract low-level features from the multi-channel input. This strategy enhances compatibility with the original architecture and stabilizes training.

Single-Scattering Baseline. A simplified version of Kajiya’s rendering equation for a surface point p and outgoing direction ω_o can be written as:

$$L_o(p, \omega_o) = \int_{\Omega} f_r(p; \omega_i, \omega_o) L_i(p; \omega_i) G_{\text{mask}}(p, \omega_i, \omega_o) (\mathbf{n} \cdot \omega_i) d\omega_i, \quad (5)$$

where f_r is a local BRDF, L_i is the incident radiance, and G_{mask} represents geometry-driven visibility or masking. For simplicity, we omit secondary bounces, subsurface scattering, and emissive effects.

Microfacet BRDF Decomposition. Under microfacet theory (e.g., Cook-Torrance), the BRDF f_r factorizes into Fresnel F , normal distribution D , and a geometric masking term G :

$$f_r(\omega_i, \omega_o; \mathbf{x}_m, \mathbf{x}_g) = \frac{F(\mathbf{x}_m, \mathbf{h}) D(\mathbf{x}_m, \mathbf{h}) G(\mathbf{x}_g, \omega_i, \omega_o)}{4 (\mathbf{n} \cdot \omega_i) (\mathbf{n} \cdot \omega_o)}, \quad (6)$$

where \mathbf{x}_m (material) includes roughness, metallic, etc., and \mathbf{x}_g (geometry) includes the macroscopic normal \mathbf{n} . Meanwhile, $L_i(\omega_i)$ may be regarded as a function of \mathbf{x}_l (e.g., environment maps, shadow buffers). Substituting Eq. (6) into Eq. (5) gives:

$$L_o = \int_{\Omega} [F(\mathbf{x}_m, \mathbf{h}) D(\mathbf{x}_m, \mathbf{h}) G(\mathbf{x}_g, \omega_i, \omega_o)] L_i(\omega_i; \mathbf{x}_l) (\mathbf{n} \cdot \omega_i) d\omega_i. \quad (7)$$

Thus, geometry (\mathbf{x}_g), material (\mathbf{x}_m), and lighting (\mathbf{x}_l) appear in separate factors, multiplying one another within the integral. This partial independence motivates a network design that processes these components in separate branches, rather than entangling them from the beginning.

Under the single-scattering assumption with microfacet BRDFs, geometry, material, and lighting parameters do not collapse into one monolithic function; instead, they appear via distinct multiplicative and additive terms. Accordingly, a factorized neural architecture (e.g., $\mathbf{n}, \mathbf{d} \rightarrow G(\cdot); \mathbf{A}, \mathbf{r}, \mathbf{m} \rightarrow M(\cdot); L_i \rightarrow L(\cdot)$; then fused) can better

align with the physical rendering process, often requiring fewer parameters and yielding more stable training.

G-buffers and Branch Networks. In practice, we store $\{\mathbf{n}, \mathbf{d}\}$ in a *geometry buffer*, $\{\mathbf{A}, r, m\}$ in a *material buffer*, and \mathbf{x}_l (irradiance, irradiance mask) in a *lighting buffer*. Our goal is to learn the mapping

$$F : (\mathbf{n}, \mathbf{d}, \mathbf{A}, r, m, \mathbf{x}_l) \mapsto \mathbf{L}_o,$$

but instead of a single network, we *factor* it into three sub-networks:

$$\mathbf{L}_o = H\left(G(\mathbf{n}, \mathbf{d}), M(\mathbf{A}, r, m), L(\mathbf{x}_l)\right), \quad (8)$$

where: $G(\cdot)$ extracts geometry-related features, $M(\cdot)$ operates on material properties, $L(\cdot)$ processes the lighting buffer, $H(\cdot)$ fuses these intermediate embeddings to predict the final \mathbf{L}_o . By respecting this tripartite factorization, our network design *mimics the physical structure* of physically based rendering (PBR) and empirically improves training stability (see Figure 4).

w/o Branch Networks w/ Branch Networks Ground truth

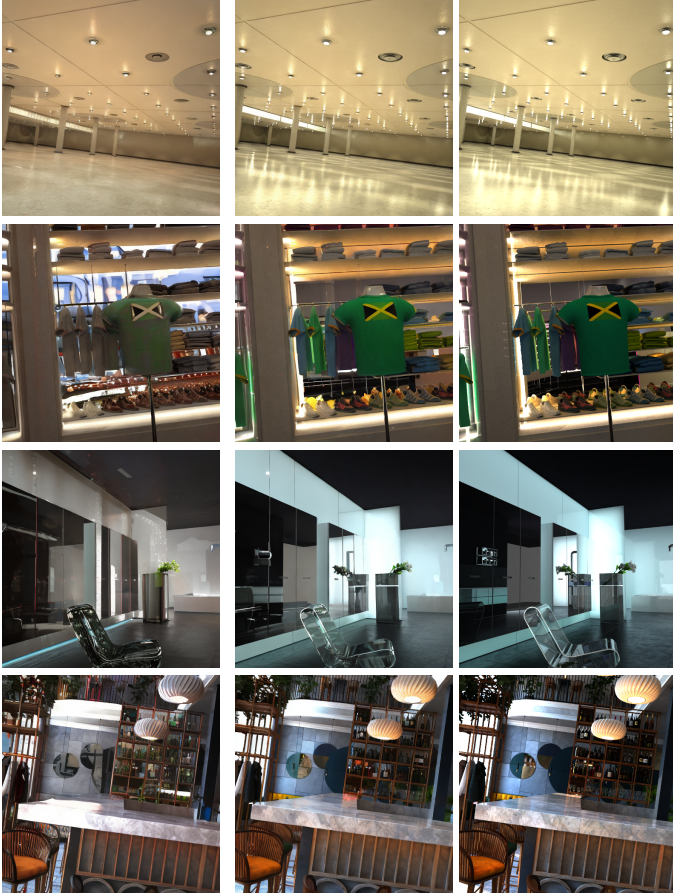


Fig. 4. Ablation of G-buffer to Final Image with or without Branch Networks. This figure illustrates the impact of Branch Networks on g-buffer rendering. Results show that including Branch Networks produces outputs more closely aligned with the ground truth. All g-buffers and ground-truth images are from the Hypersim dataset.

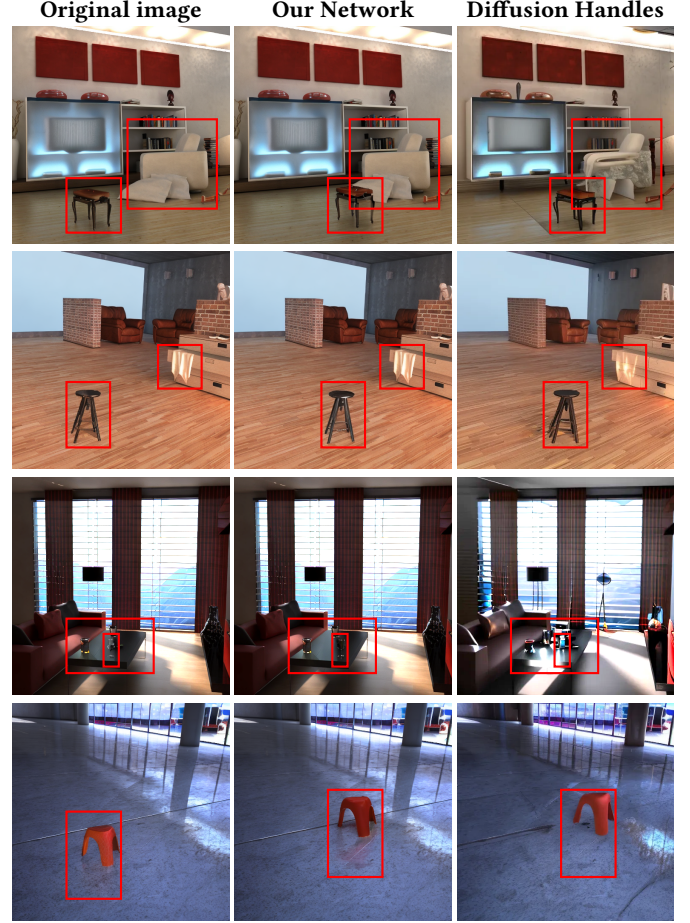


Fig. 5. Comparison with Diffusion Handle. In this figure, we compare object movement results between our method and Diffusion Handle. Our approach consistently achieves higher-quality outputs with minimal background alterations, whereas Diffusion Handle exhibits more pronounced background changes and underperforms under extreme lighting conditions.

3.3 Implementation Details

Editing and Inpainting. When performing inpainting or moving objects, we directly copy the target object into the albedo, normal, roughness, depth, and metallic channels. For the irradiance map, we fill the edited region with black (i.e., zero) to indicate that these areas need to be recalculated, and simultaneously create a mask channel. In this mask, $\text{mask}=1$ denotes unmodified regions, while $\text{mask}=0$ indicates edited regions. The same procedure applies to object movement: we update the albedo and other channels, but for the irradiance channel, the network is guided by the mask to re-estimate lighting where needed.

Dataset. The original diffusion model was trained on a corpus of around 5 billion samples, whereas our indoor-focused data is orders of magnitude smaller. To mitigate overfitting, we combine **InteriorVerse**[Zhu et al. 2022b] (over 50k samples with albedo, normal, roughness, depth, metallic) and **Hypersim**[Roberts et al. 2021] (70k+ samples with shading/irradiance but lacking roughness, metallic),

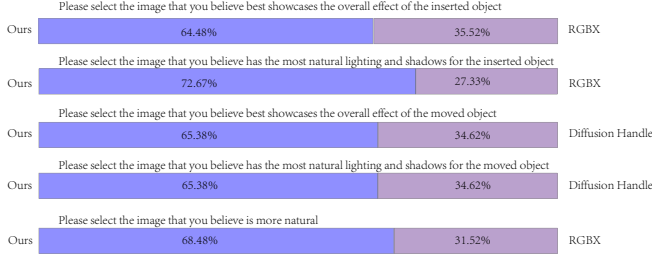


Fig. 6. s User study results (156 participants). Each bar illustrates the percentage of participants who preferred either our method or the baseline methods across various evaluation criteria. Participants compared pairs of static images generated by our method and the respective baseline (RGBX or Diffusion Handles). Three evaluation questions were utilized for comparisons with RGBX, while two questions were employed for comparisons with Diffusion Handles due to technical limitations in rendering buffers with Diffusion Handles.

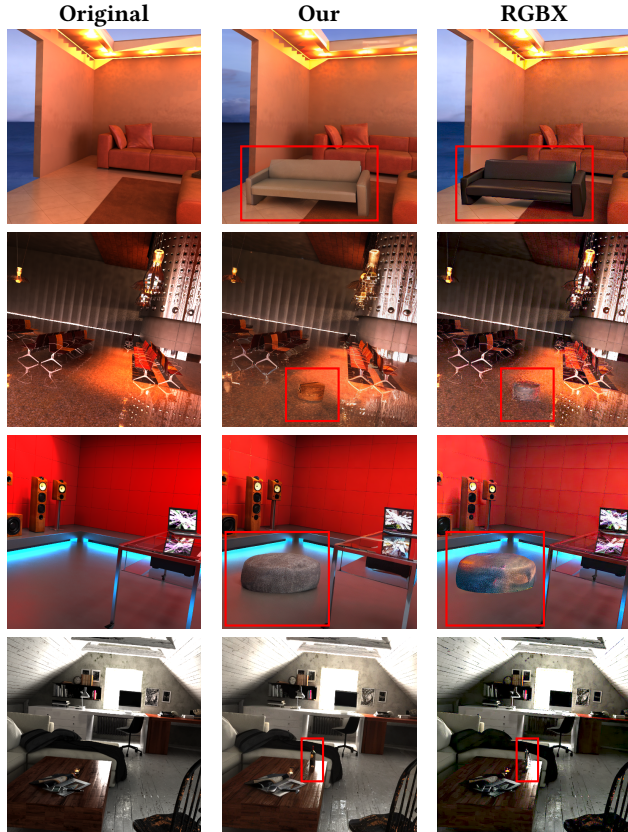


Fig. 7. Comparison with RGBX. This figure presents an inpainting comparison between our method and an RGBX-inpainting variant. The original images and inserted objects are synthetic data from the Hypersim dataset. Our approach demonstrates higher shadow quality and overall image fidelity compared to RGBX.

yielding over 120k samples in total. While still considerably smaller than 5B, this merged set allows us to adapt the network to indoor scenes. Consequently, we continue to use the partial-finetuning

strategy described in our method (Section 3.1), which preserves the broad generative capability while focusing on indoor-specific G-buffer outputs.

Training Procedure. We employ the mean squared error (MSE) as the loss function. All channels from the GBuffer are normalized to the range $[0, 1]$. Specifically, the irradiance and target images are normalized based on the 99% valid pixel range, while the depth channel undergoes logarithmic normalization. The network is trained for a total of 30 epochs. During the first 25 epochs, only the ControlNet is trained, with the main diffusion UNet kept *frozen* to preserve its large-scale generative knowledge. In the final 5 epochs, we *unfreeze* the main UNet but set its learning rate to one-fifth that of the ControlNet, thereby mitigating the risk of catastrophic forgetting. The initial learning rate is set to 5×10^{-6} with a linear decay schedule, and the batch size is 16. The entire training process, executed on 4 A100 GPUs, requires approximately 150 hours.

Mask-Guided Fine-Tuning. Note that our second-stage network (ControlNet + UNet) accepts albedo, normal, roughness, metallic, irradiance, and depth channels, plus an optional mask channel. In early epochs, the mask is set to 1 everywhere (no masking). Later, we gradually introduce regions where $\text{mask}=0$, forcing the irradiance there to be set to zero. This signals the model to re-estimate lighting in those areas, facilitating flexible edits in the final G-buffer. Once the network generates a complete G-buffer, each map (e.g. albedo, normal, roughness) can be freely edited, and for the irradiance channel specifically, we rely on the mask to indicate which parts need recomputation.

4 RESULTS AND COMPARISONS

In this section, we present multiple comparison results and ablation studies. We first showcase figures from Sections 3.1 and 3.2, followed by comparisons with existing approaches such as RGBX and Diffusion Handles. We also provide additional results demonstrating our method's efficacy in both indoor and outdoor settings.

4.1 Quantitative Evaluation

User Study and Analysis. We conducted a user study to evaluate the perceived quality and realism of our method compared to competing approaches. A total of 156 participants were recruited. Each participant completed **30 forced-choice questions**, with two images shown side-by-side in each question (our result vs. a baseline result). The participants were instructed to choose *which image they felt looked better or more visually plausible*. Each participant received the 30 questions in a randomized order to mitigate potential ordering effects. Within each question, the left-right placement of our output vs. the baseline output was also randomized to avoid positional bias. We emphasized that participants should pay attention to both local details and global consistency. Participants spent approximately 5–10 minutes to finish all 30 questions.

As shown in Figure [6], our method was preferred by 64.48% of participants over RGBX for the overall image quality. Regarding the naturalness of newly inserted objects and their shading, 72.67% of the participants deemed our results superior. In the context of moving objects where participants compared two static images depicting

objects in different positions, we received 65.38% preference for both overall effect and shading when compared to Diffusion Handles. Finally, when asked about the overall generation quality without inserting and moving objects, 68.48% of participants favored our approach. These findings suggest that our method consistently produces more realistic and visually appealing edits than the baseline approaches across various scenarios.

4.2 Ablation Study

Text-to-G-buffer Ablation. We conduct an ablation study on different strategies for text-to-G-buffer generation, illustrated in Figure 3. To ensure fair comparisons and maintain consistent outputs, all methods use the same random noise, prompt, global seed, and generator. The first row shows an RGBX[Zeng et al. 2024] network connected to a complete Stable Diffusion 2 pipeline. The second row removes ControlNet and fine-tunes only the Stable Diffusion 2 UNet on our dataset, using the same training duration. The third row employs our proposed approach: we introduce ControlNet and initially keep the Stable Diffusion model frozen, later unfreezing it at a lower learning rate.

Results indicate that **RGBX** struggles with generating accurate normal maps from outputs of stable diffusion and often fails to capture fine geometric details. By contrast, **UNet-only** fine-tuning yields moderate improvements but still struggles with fine details. In **our method**, the combination of ControlNet and partial UNet fine-tuning produces more accurate and detailed G-buffers, especially in complex scenes.

G-buffer to Final Image With/Without Branch Networks. Figure 4 compares our branch-based rendering (inspired by physically based rendering principles and employing sub-networks G , M , L , and a merge module H) against a single ControlNet trained end-to-end without such factorization. For clarity, we do not use the entire pipeline; instead, we take G-buffers directly from the dataset and feed them into the second-stage network to render images, allowing a direct comparison with ground truth.

Our physically motivated branch approach captures lighting, geometry, and material properties more consistently. In contrast, direct ControlNet training exhibits mild color mismatches (e.g., background color artifacts) and struggles with complex lighting effects (e.g., ground reflections). Transparent or highly reflective objects (glass seats, mirrors, metallic surfaces) are also rendered more accurately by our branched model. The single ControlNet baseline frequently produces metallic reflections in glass objects or overly diffuse reflections on metallic surfaces, undermining realism. Table 1 illustrates the performance improvements achieved by incorporating branch networks into our model. Specifically, the model with branch networks exhibits a significant reduction in Mean Squared Error (MSE) and Learned Perceptual Image Patch Similarity (LPIPS) scores, alongside enhancements in Structural Similarity Index Measure (SSIM) and Peak Signal-to-Noise Ratio (PSNR) metrics, compared to the model without branch networks.

4.3 Comparison with Related Work

Comparison with RGBX. Figure 7 compares our method and RGBX [Zeng et al. 2024] on inpainting tasks. To ensure fairness, we use

Table 1. Performance Comparing Models With and Without Branch Networks. ↓ indicates that lower values are better, while ↑ indicates that higher values are better.

Metric	w/o Branch Networks	w/ Branch Networks
MSE ↓	0.0288	0.0068
LPIPS ↓	0.2686	0.0973
SSIM ↑	0.6350	0.8072
PSNR ↑	15.9983	21.9883

existing G-buffers from the Hypersim dataset instead of ones generated by our network. The left column shows the original image, the middle column shows our result, and the right column is RGBX’s output.

Our method produces more natural shadows and lighting for inserted objects. By contrast, RGBX often exhibits unnatural artifacts or inaccurate color for inserted objects, especially for reflective or refractive surfaces like glass (e.g., the wine bottle in the final scene). In the second example, where a wooden stump is inserted, our method preserves refraction effects, yielding a coherent scene. RGBX fails to capture these details, leading to visually inconsistent results. In the third example, RGBX generates odd shadows, whereas ours maintains shape details and realistic shadow casting.

Comparison with Diffusion Handles. Figure 5 compares our method to a diffusion-based editing approach [Pandey et al. 2024] that specializes in moving objects within an image. We generated multiple outputs (over five) for the competing method and chose its best result for display; even so, it often distorts the background or alters object geometry. For instance, in the first image, the sofa becomes deformed when the chair is moved. In the second image, a background scarf becomes partially transparent, and in the third example, the glass object fails to maintain realistic lighting. The fourth image consistently shows unnatural floor lighting. In contrast, **our approach** preserves background details, refraction, shadow consistency, and object geometry across all examples, resulting in more reliable and practical edited outputs.

4.4 Additional Results

Figure 8 shows our *end-to-end* workflow results: a text prompt generates an indoor-scene G-buffer, which our neural renderer then converts into the final image. In Figure 9, we extend this end-to-end approach to outdoor scenes. Despite our training data being predominantly indoor, our method generalizes surprisingly well to outdoor environments, indicating robust feature representations learned in the text-to-G-buffer and rendering stages. In both results, some long prompts have been simplified. For the complete prompts and all G-buffers, please refer to the supplementary material.

5 DISCUSSION AND CONCLUSION

Limitations and Future Work. While our model supports both indoor and outdoor scenarios, it is primarily trained on an indoor-focused dataset, which can limit its performance in certain outdoor environments. In such cases, the network may occasionally yield imperfect results, particularly when dealing with complex outdoor lighting or geometric structures. Future work will explore larger and

more diverse training sets to improve generalization and address these remaining shortcomings.

Conclusion. In summary, our method combines screen-space rendering with diffusion models to offer greater control over image generation. We propose a two-stage architecture: a frozen diffusion model with a ControlNet to produce a G-buffer from text prompts, followed by a rendering network—also featuring a ControlNet—to generate the final image. By introducing sub-networks to handle geometry, materials, and lighting channels, we incorporate physically based rendering principles. Freezing the primary diffusion model early on and later fine-tuning it with a smaller learning rate preserves the broad capabilities of large-scale pre-training while adapting to our smaller dataset. This structured approach enhances training stability, facilitates editability, and extends to a variety of scenes.

REFERENCES

- Jonathan T. Barron, Ben Mildenhall, Dor Verbin, Pratul P. Srinivasan, and Peter Hedman. 2022. Mip-NeRF 360: Unbounded Anti-Aliased Neural Radiance Fields. In *2022 IEEE/CVF Conference on Computer Vision and Pattern Recognition (CVPR)*. 5460–5469. <https://doi.org/10.1109/CVPR52688.2022.00539>
- Chris Buehler, Michael Bosse, Leonard McMillan, Steven Gortler, and Michael Cohen. 2001. Unstructured lumigraph rendering. In *Proceedings of the 28th Annual Conference on Computer Graphics and Interactive Techniques (SIGGRAPH '01)*. Association for Computing Machinery, New York, NY, USA, 425–432. <https://doi.org/10.1145/383259.383309>
- Prafulla Dhariwal and Alex Nichol. 2021. Diffusion models beat GANs on image synthesis. In *Proceedings of the 35th International Conference on Neural Information Processing Systems (NIPS '21)*. Curran Associates Inc., Red Hook, NY, USA, Article 672, 15 pages.
- David Griffiths, Tobias Ritschel, and Julien Philip. 2022. OutCast: Single Image Relighting with Cast Shadows. *Computer Graphics Forum* 43 (2022).
- Peter Hedman, Julien Philip, True Price, Jan-Michael Frahm, George Drettakis, and Gabriel Brostow. 2018. Deep blending for free-viewpoint image-based rendering. *ACM Trans. Graph.* 37, 6, Article 257 (Dec. 2018), 15 pages. <https://doi.org/10.1145/3272127.3275084>
- Stephen Lombardi, Tomas Simon, Jason Saragih, Gabriel Schwartz, Andreas Lehrmann, and Yaser Sheikh. 2019. Neural volumes: learning dynamic renderable volumes from images. *ACM Trans. Graph.* 38, 4, Article 65 (July 2019), 14 pages. <https://doi.org/10.1145/3306346.3323020>
- Ben Mildenhall, Pratul P. Srinivasan, Matthew Tancik, Jonathan T. Barron, Ravi Ramamoorthi, and Ren Ng. 2021. NeRF: representing scenes as neural radiance fields for view synthesis. *Commun. ACM* 65, 1 (Dec. 2021), 99–106. <https://doi.org/10.1145/3503250>
- Oliver Nalbach, Sebastian Seda, Christian Torbach, and Arno Magnus. 2017. Deep Shading: Convolutional Neural Networks for Screen-Space Shading. In *Proceedings of the Eurographics Symposium on Rendering (EGSR)*.
- Alexander Quinn Nichol, Prafulla Dhariwal, Aditya Ramesh, Pranav Shyam, Pamela Mishkin, Bob McGrew, Ilya Sutskever, and Mark Chen. 2022. GLIDE: Towards Photorealistic Image Generation and Editing with Text-Guided Diffusion Models. In *Proceedings of the 39th International Conference on Machine Learning (Proceedings of Machine Learning Research, Vol. 162)*, Kamalika Chaudhuri, Stefanie Jegelka, Le Song, Csaba Szepesvari, Gang Niu, and Sivan Sabato (Eds.). PMLR, 16784–16804. <https://proceedings.mlr.press/v162/nichol22a.html>
- Karran Pandey, Paul Guerrero, Matheus Gadelha, Yannick Hold-Geoffroy, Karan Singh, and Niloy J Mitra. 2024. Diffusion Handles Enabling 3D Edits for Diffusion Models by Lifting Activations to 3D. In *Proceedings of the IEEE/CVF Conference on Computer Vision and Pattern Recognition*. 7695–7704.
- Rohit Pandey, Sergio Orts Escolano, Chloe Legendre, Christian Häne, Sofien Bouaziz, Christoph Rhemann, Paul Debevec, and Sean Fanello. 2021. Total relighting: learning to relight portraits for background replacement. *ACM Trans. Graph.* 40, 4, Article 43 (July 2021), 21 pages. <https://doi.org/10.1145/3450626.3459872>
- Keungho Park, Utkarsh Sinha, Jonathan T. Barron, Sofien Bouaziz, Dan B Goldman, Steven M. Seitz, and Ricardo Martin-Brualla. 2021. Nerfies: Deformable Neural Radiance Fields. *ICCV* (2021).
- Eric Penner and Li Zhang. 2017. Soft 3D reconstruction for view synthesis. *ACM Trans. Graph.* 36, 6, Article 235 (Nov. 2017), 11 pages. <https://doi.org/10.1145/3130800.3130855>
- Dustin Podell, Zion English, Kyle Lacey, Andreas Blattmann, Tim Dockhorn, Jonas Müller, Joe Penna, and Robin Rombach. 2023. Sdxl: Improving latent diffusion models for high-resolution image synthesis. *arXiv preprint arXiv:2307.01952* (2023).
- Aditya Ramesh, Mikhail Pavlov, Gabriel Goh, Scott Gray, Chelsea Voss, Alec Radford, Mark Chen, and Ilya Sutskever. 2021. Zero-Shot Text-to-Image Generation. In *Proceedings of the 38th International Conference on Machine Learning (Proceedings of Machine Learning Research, Vol. 139)*, Marina Meila and Tong Zhang (Eds.). PMLR, 8821–8831. <https://proceedings.mlr.press/v139/ramesh21a.html>
- Scott Reed, Zeynep Akata, Xinchun Yan, Lajanugen Logeswaran, Bernt Schiele, and Honglak Lee. 2016. Generative adversarial text to image synthesis. In *Proceedings of the 33rd International Conference on International Conference on Machine Learning - Volume 48* (New York, NY, USA) (ICML '16). JMLR.org, 1060–1069.
- Mike Roberts, Jason Ramapuram, Anurag Ranjan, Atulit Kumar, Miguel Angel Bautista, Nathan Paczan, Russ Webb, and Joshua M. Susskind. 2021. Hypersim: A Photorealistic Synthetic Dataset for Holistic Indoor Scene Understanding. In *International Conference on Computer Vision (ICCV)* 2021.
- Robin Rombach, Andreas Blattmann, Dominik Lorenz, Patrick Esser, and Bjorn Ommer. 2022. High-Resolution Image Synthesis with Latent Diffusion Models. In *2022 IEEE/CVF Conference on Computer Vision and Pattern Recognition (CVPR)*. IEEE Computer Society, Los Alamitos, CA, USA, 10674–10685. <https://doi.org/10.1109/CVPR52688.2022.01042>
- Viktor Rudnev, Mohamed Elgharib, William Smith, Lingjie Liu, Vladislav Golyanik, and Christian Theobalt. 2022. NeRF for Outdoor Scene Relighting. In *European Conference on Computer Vision (ECCV)*.
- Chitwan Saharia, William Chan, Saurabh Saxena, Lala Lit, Jay Whang, Emily Denton, Seyed Kamyar Seyed Ghasemipour, Burcu Karagol Ayan, S. Sara Mahdavi, Raphael Gontijo-Lopes, Tim Salimans, Jonathan Ho, David J Fleet, and Mohammad Norouzi. 2022. Photorealistic text-to-image diffusion models with deep language understanding. In *Proceedings of the 36th International Conference on Neural Information Processing Systems (New Orleans, LA, USA) (NIPS '22)*. Curran Associates Inc., Red Hook, NY, USA, Article 2643, 16 pages.
- Daniel Thomas and Angus Forbes. 2018. Deep Illumination: A Conditional Generative Adversarial Network for Predicting Indirect Lighting. In *Proceedings of ACM SIGGRAPH Asia*.
- Edgar Tretschk, Ayush Tewari, Vladislav Golyanik, Michael Zollhöfer, Carsten Stoll, and Christian Theobalt. 2020. PatchNets: Patch-Based Generalizable Deep Implicit 3D Shape Representations. In *Computer Vision – ECCV 2020*, Andrea Vedaldi, Horst Bischof, Thomas Brox, and Jan-Michael Frahm (Eds.). Springer International Publishing, Cham, 293–309.
- Zian Wang, Tianchang Shen, Jun Gao, Shengyu Huang, Jacob Munkberg, Jon Hasselgren, Zan Gojic, Wenzheng Chen, and Sanja Fidler. 2023. Neural Fields meet Explicit Geometric Representations for Inverse Rendering of Urban Scenes. In *The IEEE Conference on Computer Vision and Pattern Recognition (CVPR)*.
- Tao Xu, Pengchuan Zhang, Qiuyuan Huang, Han Zhang, Zhe Gan, Xiaolei Huang, and Xiaodong He. 2018. AttnGAN: Fine-Grained Text to Image Generation with Attentional Generative Adversarial Networks. In *2018 IEEE/CVF Conference on Computer Vision and Pattern Recognition*. 1316–1324. <https://doi.org/10.1109/CVPR.2018.00143>
- Bowen Xue, Claudio Guarnera, Shuang Zhao, and Zahra Montazeri. 2024. Reflectance-Fusion: Diffusion-based text to SVBRDF Generation. In *Eurographics Symposium on Rendering*. Eurographics Association.
- Ye Yu, Abhimeta Meka, Mohamed Elgharib, Hans-Peter Seidel, Christian Theobalt, and Will Smith. 2020. Self-supervised Outdoor Scene Relighting. In *European Conference on Computer Vision (ECCV)*.
- Zheng Zeng, Valentin Deschaintre, Iliyan Georgiev, Yannick Hold-Geoffroy, Yiwei Hu, Fujun Luan, Ling-Qi Yan, and Miloš Hašan. 2024. Rgb-x: Image decomposition and synthesis using material-and lighting-aware diffusion models. In *ACM SIGGRAPH 2024 Conference Papers*. 1–11.
- Han Zhang, Tao Xu, Hongsheng Li, Shaoting Zhang, Xiaogang Wang, Xiaolei Huang, and Dimitris Metaxas. 2017. StackGAN: Text to Photo-Realistic Image Synthesis with Stacked Generative Adversarial Networks. In *2017 IEEE International Conference on Computer Vision (ICCV)*. 5908–5916. <https://doi.org/10.1109/ICCV.2017.629>
- Yalan Zhang, Yuhang Xu, Yanrui Xu, Yue Hou, Xiaokun Wang, Yu Guo, Mohammad S. Obaidat, and Xiaojuan Ban. 2024. Real-time screen space rendering method for particle-based multiphase fluid simulation. *Simulation Modelling Practice and Theory* 136 (2024), 103008. <https://doi.org/10.1016/j.simpat.2024.103008>
- Jingsen Zhu, Fujun Luan, Yuchi Huo, Zihao Lin, Zhihua Zhong, Dianbing Xi, Rui Wang, Hujun Bao, Jiaxiang Zheng, and Rui Tang. 2022a. Learning-based Inverse Rendering of Complex Indoor Scenes with Differentiable Monte Carlo Raytracing. In *SIGGRAPH Asia 2022 Conference Papers* (Daegu, Republic of Korea) (SA '22). Association for Computing Machinery, New York, NY, USA, Article 6, 8 pages. <https://doi.org/10.1145/3550469.3555407>
- Jingsen Zhu, Fujun Luan, Yuchi Huo, Zihao Lin, Zhihua Zhong, Dianbing Xi, Rui Wang, Hujun Bao, Jiaxiang Zheng, and Rui Tang. 2022b. Learning-Based Inverse Rendering of Complex Indoor Scenes with Differentiable Monte Carlo Raytracing. In *SIGGRAPH Asia 2022 Conference Papers*. ACM, Article 6, 8 pages. <https://doi.org/10.1145/3550469.3555407>



Minimalist workspace featuring a floating desk with plants, a laptop, and a modern wooden chair



Rustic storage bench with woven baskets, white blankets, and a vase of fresh flowers, set against a wooden shiplap wall



Elegant bedroom with a tufted blue headboard, pastel pink bedding, floral wallpaper, and wooden bedside tables



Elegant bedroom with a soft gray palette, layered pillows, a sleek bedside lamp, and minimalist decor



Cozy indoor garden nook with hanging plants, a wooden bench with colorful cushions, and lush greenery by a bright window



Serene indoor corner with a wooden armchair, soft gray cushions, and tall potted plants creating a lush, natural vibe



Modern reading nook with built-in shelves, cushioned seating, and neatly arranged books and decor, framed by soft curtains



Organized laundry shelf with woven baskets, folded towels, and neatly arranged items



Minimalist nursery with a white crib, changing table, fluffy rug, and soft beige curtains



Modern bedroom with soft ambient lighting, a cozy upholstered bed, textured walls, and a plush area rug



Stylish reading corner with a patterned armchair, round wooden side table, and lush indoor plant by sheer curtains



Well-organized woodworking workshop with tools hanging on the wall, a sturdy workbench, and wooden storage shelves



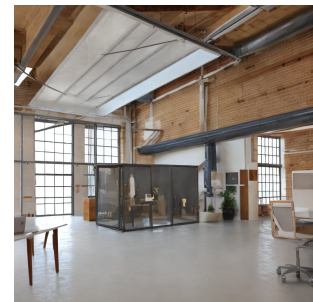
A cozy reading alcove under the stairs with built-in bookshelves and soft cushions



A pastel-toned bedroom featuring a tufted headboard and floral-patterned bedding

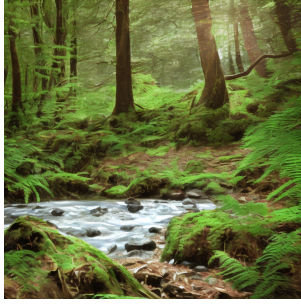


A sophisticated living space featuring marble floors and floor-to-ceiling drapes



A modern loft office space bathed in natural light from large skylights

Fig. 8. Additional result indoor



Sunlit forest clearing with a gentle stream, surrounded by lush green ferns and tall trees, creating a serene and natural atmosphere.



Peaceful forest campsite with blue and red tents surrounded by tall pine trees, creating a cozy and natural outdoor setting.



Medieval stone courtyard with tall cylindrical towers, arched wooden door, ivy-covered walls, and a simple bench on a cobblestone floor



Serene bamboo forest with a winding wooden pathway surrounded by tall green bamboo stalks and natural fences.



Vast lavender fields in full bloom with vibrant purple rows, bordered by green hedges and rolling hills in the background under a soft sky.



Sunny park with lush greenery, colorful flower beds, people walking, and exercise equipment along a paved pathway



Zen garden with a bonsai tree in a ceramic pot, surrounded by moss-covered rocks, white gravel, and carefully arranged stones.



Mountain landscape with snowy peaks, green meadows, and a dirt path splitting into two directions under a clear blue sky.



Ancient stone amphitheater overlooking lush terraced hills and a vast scenic landscape under a clear sky.



Charming Mediterranean courtyard with white walls, bright blue doors and windows, pink bougainvillea, and outdoor seating.



Majestic mountain valley with a turquoise glacial river winding through rugged terrain, surrounded by misty peaks and cloudy skies.



Elegant French-style castle garden with symmetrical hedges, manicured greenery, and a historic stone castle in the background.

Fig. 9. Additional result outdoor